

A diffusion weighted informed model of the rabbit gastrocnemius

M Alipour¹, K Mithraratne¹, J Fernandez^{1,2}

1. Auckland Bioengineering Institute, University of Auckland, NZ

2. Department of Engineering Science, Auckland University, NZ

Submitted as an **Original Article** to the Journal

Annals of Biomedical Engineering, 2015

Address correspondence to:

Justin W Fernandez

Auckland Bioengineering Institute

The University of Auckland, New Zealand

Email: j.fernandez@auckland.ac.nz

Phone: +64 9 373 7599 ext 89196

Running title: A diffusion weighted informed rabbit gastrocnemius model

Abstract

2 The NZ white rabbit is the animal of choice for much experimental work due to its
muscular frame; similar response to human diseases; and is one of the few mammals that have
4 had their genome sequenced. However, computational models of rabbit muscle detailing fibre
architecture are limited in the literature, especially the gastrocnemius, which has similar
6 biomechanics and translatable findings to the human. This study presents a geometrical model of
the rabbit gastrocnemius informed with Diffusion Weighted Imaging (DWI) based fibres.
8 Passive material properties are estimated using known muscle deformation inferred from
Magnetic Resonance imaging (MRI) data and dorsiflexion force measured with a custom built
10 rabbit rig and transducer. Muscle shape prediction is evaluated against a second rabbit. This
study revealed that the gastrocnemius steady-state force post rigor is close to *in vivo* for small
12 deformations but increases by a fixed ratio as the deformation increases and can be used to
evaluate the passive behaviour of muscle. DW fibre orientation significantly influences shape
14 and mechanics during muscle contraction. The presented gastrocnemius force and material
properties may be used to inform the constitutive behaviour of rabbit models used to investigate
16 pathology and musculotendon treatments that may be translated to the human condition.

18 Key words: DWI; DTI; muscle fibres; rabbit gastrocnemius, rabbit force rig;

20

22

Introduction

2 The New Zealand white rabbit is the animal of choice for both experimental and
computational work. It has a similar response to human diseases; and is one of the few mammals
4 to have had their genome sequenced [1]. The rabbit's lower hind limb has four major muscles
similar to the human, namely, the gastrocnemius (medial and lateral heads), soleus and tibialis
6 anterior. However, unlike humans, the rabbit hind limb has only one supporting bone, the tibia.
For this study we have focussed on the gastrocnemius muscle, which originates in the femoral
8 condyles and inserts in the calcaneus (heel bone) via the Achilles tendon. Computational models
of rabbit muscle detailing fibre architecture are limited in the literature, especially the
10 gastrocnemius, which has similar mechanics and translatable findings to the human. Rabbits are
also used as models for investigating joint weakness leading to osteoarthritis (OA) Herzog and
12 Longino [2].

 There are rigid body models of the NZ white rabbit with line muscle actuators [3] but
14 these do not evaluate the influence of 3D fibrous architecture on spatially varying muscle stress
and strain. The macro level material properties of the rabbit have been shown to be a scalable
16 version of the sarcomeres in rabbit hind limb muscles [4]. Passive muscle force has previously
been measured using a fibre optic pressure transducer in the tibialis anterior of 12 NZ rabbits [5],
18 and for static and dynamic loading in both female and male rabbits [6]. Failure sites and peak
tensile forces of the composite triceps surae in 24 NZ white rabbits were identified during
20 passive extension [7]. One of the only studies in the literature that reports the post-mortem
effects in NZ white rabbits was Van Ee and colleagues [8]. They showed a distinct steady state
22 post rigor phase which was repeatable and the failure strain was unchanged from *in vivo*.

DWI [9] is an MR imaging sequence used to map the architecture of fibres in muscle [10, 11] and neuronal pathways in cerebral tissue [12, 13]. The concept is that the dominant diffusion direction of fluid relates to the fibre direction in muscle. DWI has been used to examine the diffusive properties of adjacent muscles at rest in the human gastrocnemius [14] and to identify properties of healthy and damaged muscles [15, 16]. Van Donkelaar et al. [17] used DWI to obtain geometric information for numerical simulations of skeletal muscle contractions. Their results showed that DWI provided enough resolution and accuracy to use DWI based fibre directions in biomechanical analyses.

One of the challenges present in this study was that muscle enters rigor and so material properties are changing dynamically following euthanasia. This makes it difficult to measure muscle force over four positions and have the muscle stable for MR imaging. Van Ee et al. [8] reported the post-mortem effects in twelve NZ white rabbits following euthanasia and we used this information in the design of our experiments as we could not measure force and MR image while the muscle was going through changes due to rigor mortis. Following euthanasia, Van Ee and colleagues exposed the rabbit tibialis anterior muscle by an anterior midline incision from the knee to the ankle. All supporting connective tissue and fascia were removed. In that study, they performed an elongation test every hour post-mortem up to 18 hours and then every 2 hours until 72 hours after death. The key point from this study was that after rigor passed the failure strain was relatively constant and not much higher than *in vivo*.

The objectives of this study were to firstly present measured passive gastrocnemius force in the NZ white rabbit from death throughout rigor mortis to post-rigor using a novel rabbit rig. This information is used to relate the post-rigor to *in vivo* force and give a surrogate estimate of the active muscle contraction (the peak during rigor mortis). Secondly we present optimised

passive material properties determined from force measurement and MRI shape accounting for
2 fibrous muscle architecture. We also evaluate the error in the system using a celery-based
phantom. Thirdly, we present the influence that DW fibres have on muscle contractile shape and
4 mechanics.

6 **Materials and Methods**

MR compatible rabbit rig

8 A custom rabbit rig was designed in SolidWorks (Dassault Systems) and is shown in
Figure 1. The key components of the rig included four clamps to constrain the limbs, a variable
10 shaft to control rabbit length, a variable angle drive to control hind limb dorsiflexion (which was
measured using a protractor), a ring with screws to rigidly fix the femur bone and two tendon
12 clamps, which integrated with a custom built force transducer. The rig was printed using a 3D
printer (Stratasys®) at a resolution of 100 microns using ABSplus material. The key design
14 features of this rabbit rig were the abilities to hold multiple size rabbits up to 5 kg, able to be
operated by a single person, MR compatible, strong enough to cope with muscle rigor and
16 designed to fit in the 4.7 T animal MRI housed at the Centre for Advanced MRI (CAMRI) at
Auckland University.

18 **Force transducer**

Two capacitive sensors were designed to measure two distinct ranges of force; 0.00098 -
20 9.80 N, and 0.0098 – 68 N, respectively, and cope with rabbits ranging from 1.5 kg to 4.0 kg,
especially during muscle rigor. Due to metallic components in the transducer, a dummy MR
22 compatible clamp was used during imaging.

Rabbit euthanasia

2 Animal ethics approval was received for 3 years from the University of Auckland animal
ethics committee (#T958) and training in rabbit handling and euthanasia was undertaken. Two
4 rabbits were euthanised, 3.8 kg and 4.2 kg in weight, respectively, using 2 ml of pentobarbital
via injection into the ear vein monitored until cessation of all signs of life. Upon cessation the
6 rabbit lower limb was flayed and the triceps surae muscle complex was exposed as shown in
Figure 2. The lower section of the tendon (inserting into the calcaneus) was cut and the
8 transducer was inserted by connecting the two sections of the tendon. The rabbit was positioned
in the rig and screws were inserted into the femur to fix the rabbit and the foot placed in the
10 adjustable leg clamp.

Rabbit passive gastrocnemius force

12 In order to avoid the dynamic changing stiffness of muscle due to rigor we adopted an
14 approach whereby rigor mortis was allowed to pass and then we measured the steady state
passive material properties. This idea was observed from the study of Van Ee et al. [8] where
16 there was a well-defined ratio between the post rigor and *in vivo* passive states. The passive
gastrocnemius force via the Achilles tendon was measured every hour for the first five hours
18 followed by every two hours up to 72 hours. Each measurement was repeated three times and the
result averaged. This process was repeated for four dorsiflexion positions (15°, 30°, 45° and
20 60°). After 72 hours rigor passed and the muscle behaviour was stable and related to the *in vivo*
force by a well-defined ratio.

22

Rabbit geometric model

2 Following measurement of passive force the geometries of the rabbit gastrocnemius
muscle were imaged using T1-weighted, MR imaging on a 4.7 T Siemens' machine with settings
4 given in Table 1. The goal of this step was to create four gold standard experimental muscle
boundaries to inform the muscle parameter optimisation. After imaging the rabbit in four
6 positions (Figures 2(I) – 2(V)), we identified the muscle and bone boundaries for segmentation
and data creation. These images were loaded into the Zinc digitiser developed as part of CMGUI
8 (www.cmiss.org) and shown in Figure 2(VI). The MR images were segmented and a 3D cloud of
data points were created for each muscle and the bone of the rabbit lower limb. These data points
10 were then used to create subject-specific finite element models of the muscles using high-order
cubic Hermite elements. The mesh creation steps are outlined in Figure 3. (i) From the cloud of
12 points (yellow data) a subset was chosen as surface nodes (red points); (ii) An initial trilinear
mesh was then built on this that captured the primary shape; (iii) Using the least squares fitting
14 procedure developed in CMISS we fitted the cubic Hermite elements [18] to a root mean square
(RMS) error of less than 2 mm. These steps were repeated for all four deformed positions of the
16 muscle plus one relaxed position without any force.

Diffusion weighted fibre field

18 The rabbit gastrocnemius was re-scanned using a DWI sequence to track the water
migration in the muscle and estimate the fibre architecture. The DWI sequence was run with the
20 parameters in Table 2, specifically, we used a b-value of 500 s.mm^{-2} for skeletal muscle and 20
gradient directions plus one reference sequence with no diffusion. The diffusion at each voxel
22 was solved using the Stejskal-Tanner relation [19], which relates the signal intensity, S , to the
diffusion tensor, \mathbf{D} , through:

$$S_k = S_0 e^{b g_k^T \mathbf{D} g_k}, \quad (1)$$

2 where S_0 is the signal intensity without the diffusion weighting, S_k is the signal intensity in the k^{th}
 3 direction, g_k is the k^{th} direction vector, b is a parameter that controls the amount of diffusion
 4 allowed (with $b=0$ being no diffusion) and \mathbf{D} is the symmetric diffusion tensor, which has six
 5 unique components to solve for at each image voxel. As we have 20 directions we adopt the
 6 least squares approach to solve for \mathbf{D} and this form is given in equation 2 as:

$$D_j = \sum_{k=1}^N (W_{kj})^{-1} \times \ln \frac{S_k}{S_0}, \quad (2)$$

8 where \mathbf{D} is solved for each of the six components ($j=1$ to 6) and W is the matrix of weights,
 9 which has six columns for each direction k and is given in equation 3 as

$$W_{kj} = b [g_{1k}^2 \quad 2g_{1k}g_{2k} \quad 2g_{1k}g_{3k} \quad g_{2k}^2 \quad 2g_{2k}g_{3k} \quad g_{3k}^2], \quad (3)$$

10 Since each voxel can be muscle, fat or background, a background grey threshold of 30 (range
 11 from 0 to 255) is used to filter white noise. The muscle voxels only within the muscle boundary
 12 were then isolated. The computed diffusion tensor (\mathbf{D}) for each muscle voxel was then
 13 diagonalised into three eigenvectors (λ_1 to λ_3) where λ_1 , the largest eigenvector, was assumed to
 14 align with fibre orientation. Secondly we used the fractional anisotropy (FA) factor [20] to
 15 isolate out tissue that is more likely muscle (striated with fibres) and filter out tissue that is most
 16 likely fat or water (have less dominant fibres). The FA measures in 3D is given by equation 4 as:

$$FA = \sqrt{\frac{1}{2} \frac{\sqrt{(\lambda_1 - \lambda_2)^2 + (\lambda_2 - \lambda_3)^2 + (\lambda_1 - \lambda_3)^2}}{\sqrt{(\lambda_1^2 + \lambda_2^2 + \lambda_3^2)}}}, \quad (4)$$

FA is a dimensionless measure between 0 and 1; where a zero value means that the tensor is represented by a sphere (where there is no dominant diffusion direction) and 1 means that the ellipsoid is a tube (which is the upper limit and has the maximum possible diffusion direction). A FA of 0.3 or greater gave a good balance between useful fibre information and filtering out much of the unwanted background tissue data. The fibre vector information was then fitted to the muscle geometry as a fibre field using the same least squares fitting technique. To evaluate the error in the DWI pipeline a phantom made of celery was used to assess the error in fibre estimation.

10 **Constitutive law fitting**

The reference pose geometry was strained using a finite elastic simulation in CMISS (www.cmiss.org) using musculotendon force measured via the transducer. The governing mechanics concerning finite elasticity and the Hill type model used for active contraction is given in Appendix A. Specifically, the peak passive force measured during rigor mortis was used as a surrogate of the maximum active contractile force. A structurally based constitutive law previously used for passive cardiac and skeletal muscle, the ‘pole-zero’ relation [21], was adopted and is defined in Equation 5 as:

$$18 \quad W = k_{\alpha\beta} \frac{E_{\alpha\beta}^2}{\left| a_{\alpha\beta} - E_{\alpha\beta} \right|^{b_{\alpha\beta}}}, \quad (5)$$

where the strain energy density function, W is defined by a asymptote function with $k_{\alpha\beta}$ the scaling function, $b_{\alpha\beta}$ curvature control, $a_{\alpha\beta}$ a strain limiting pole and $E_{\alpha\beta}$ the Green’s strain components. The model was treated as transversely isotropic with the fibre direction $\alpha=\beta=1$ aligned to the DWI fibre direction. After choosing an initial guess for the pole-zero parameters

we used the ‘fmincon’ function in the Matlab Optimisation Toolbox [22] to optimally choose parameters that minimised the difference between the mechanically deformed muscle geometry and the ‘gold standard’ geometric shape captured from MRI for each position. We optimised the pole ($a_{\alpha\beta}$) and scaling ($k_{\alpha\beta}$) parameters and fixed the curvature ($b_{\alpha\beta}$) for the fibre and transverse directions. The curvature was set to 1.0 based on previous experience with cardiac [21] and skeletal tissues [23]. We set a bound on the solution space for $a_{\alpha\beta}$ as 0.01 to 5.0 and for $k_{\alpha\beta}$ as 0.01 to 0.7 MPa. An initial guess was obtained from trials based on previous skeletal muscles [23]. This was performed until the RMS error between the computationally deformed muscle (red) and MR derived muscle (gold) was less than 2 mm (Figure 4).

Results

The passive gastrocnemius force over four dorsiflexion positions (P1 to P4) are presented in Figure 5. The shape of the passive force curve for both rabbits following the euthanasia point (EP) was characterised by a sharp rise to a peak force followed by a sharp decline and finally steady state after ~36 hours. Specifically, following euthanasia a short period of steady muscle properties lasted for ~3.6 hours before the rapid rigor onset point (ROP). The rate of increase towards peak rigor force (PR) increased with dorsiflexion position (P1 to P4). Rates of force increase from ROP to PR were 0.34 N/h for 15° dorsiflexion, 0.62 N/h for 30°, 1.18 N/h for 45° and 2.3 N/h for 60°. Steady state passive force was achieved after 36 hours and the average passive force at steady state was 0.8 N, 2.1 N, 7.9 N and 19.0 N from P1 to P4 for the average rabbit weight of 4 kg. The passive steady state (SS) rigor force was 10% larger than *in vivo* at P1 and 14%, 75% and 108% larger at positions P2 to P4, respectively. These ratios are used to relate the post-rigor force with the *in vivo* force just prior to death. The peak values were used as a

surrogate for maximum contraction in the model and were 4.8 N, 8.7 N, 20.8 N and 39.5 N from P1 to P4 for the average rabbit weight of 4 kg. The increase in peak force is influenced by the dorsiflexion angle and hence musculotendon length.

The optimal pole-zero model parameters for the rabbit gastrocnemius muscle assuming transversely isotropic behaviour are presented in Table 3. The curvature $b_{\alpha\beta}$ was set to 1.0 for all 3 directions. We found that in the fibre direction, the optimised pole (a_{11}) and scaling (k_{11}) were 1.0 and 0.01 MPa, respectively. In the transverse directions the optimised pole (a_{22} & a_{33}) and scaling (k_{22} & k_{33}) were 0.097 and 0.221 MPa, respectively. This produced an overall RMS error of 1.49 mm across all four positions (Table 4, column 1). The constitutive law was evaluated through prediction of passive shape of a second rabbit across all four positions. We used the optimised constitute parameters from the first rabbit to predict the shape of a second rabbit of similar size by loading it with the rabbit rig measured force. The average RMS error between the predicted muscle shape and MRI measured shape for all positions was 1.65 mm for the second rabbit (Table 4, column 2).

The influence of fibre orientation on predicted shape and mechanics is observed in Figures 6 and 7 as part of an isometric contraction simulation (Appendix A). Inclusion of DWI-based fibres produced a different shape during contraction, specifically; the muscle contracted more posteriorly and was directed inwards towards the central tendon as dictated by the fibre alignment. In contrast, the control model with parallel fibres simply moved superiorly and inferiorly. Both models conserved volume during deformation. The maximum error was up to 3.7 mm in shape. A perturbation of 10% in the fibre angles produced up to 1.3 mm change in surface RMS error. Strains in 3D are observed using the largest principal component vector of strain. In the DWI muscle model principal strain components are shown to align with the fibre

pennation angle and in the parallel model they are aligned with the assumed control parallel fibres. The DWI muscle also exhibits larger non-uniform strain on the medial head, which is the largest side of the gastrocnemius and has higher local contraction.

For evaluation of the fibre estimation method using DWI, we developed a gold standard phantom made from celery which has a distinct parallel fibre configuration. In the phantom, we fixed the celery using known angles followed by filling the container fully with water. This was necessary because DWI needs a fluid medium and the pockets of air create artefacts. Following the fibre fitting process the resulting DWI fibre vectors were aligned in the meshed celery as shown in Figure 8. We then compared this with the gold standard parallel-based fibres to work out the vector angle error. A maximum error of 4.6° in fibre angle occurred on the outside of the celery phantom closest to the boundary of the container. The background threshold intensity (indexed from 0 to 256) and the white matter threshold taken as the fractional anisotropy (FA defined in equation 4) was used to minimise the fibre angle error. A background threshold greater than 90 combined with a white matter FA greater than 0.1 gave the lowest error across the celery geometry. The side closest to the water boundary had the highest error (shown in red). It was found that the error was most sensitive to the FA leading to high errors propagating towards the centre of the celery when the FA was increased.

To evaluate, which parameters the model was most sensitive to we perturbed the pole zero parameters (scaling coefficient, pole and curvature) by 10% for each axis (fibre, sheet and sheet-normal) and the results are reported in Table 5. It was observed that the model was most sensitive in all 3 directions to the strain limiting pole ($a_{\alpha\beta}$) but this was most evident in the sheet and sheet-normal directions. A perturbation of 10% in the pole parameter produced a geometric RMS error in muscle shape of 0.27%, 11.18% and 14.15% for the fibre, sheet and sheet-normal

directions, respectively. The second main error was due to changes in curvature, where a 10%
2 perturbation in the curvature parameter produced a geometric RMS error in muscle shape of
1.67% and 0.97% for the sheet and sheet-normal directions, respectively. Note that the fibre
4 direction was numerically indifferent to this parameter. The scaling parameter produced errors of
less than 0.65% across all the directions (excluding the fibre orientation).

6 **Discussion**

We have presented a framework for estimating material parameters of muscle
8 (demonstrated for the rabbit) from MRI shape and measured musculotendon force using a
custom rig. The 3D printed rig was shown to be both sufficient in handling the muscle in rigor
10 and be non-ferrous and MRI compatible. Passive muscle shapes integrated with measured
musculotendon force were shown to be suitable for optimising strain behaviour. We have
12 demonstrated this by fitting a set of parameters to a muscle-based constitutive law previously
used for cardiac and skeletal muscle; the pole zero law. It was shown DWI based fibres produce
14 significantly different contractile shape, strain compared to parallel-fibre based models and the
strain patterns were spatially non-uniform and aligned with the fibre orientation. Passive muscle
16 constitutive parameters were optimised against shape and force and shown to predict the
behaviour of a second rabbit of similar size. A celery phantom was used to quantify a maximum
18 error of 4.6° in our DWI fibre based angle estimation and modelling pipeline.

There are a number of limitations that should be considered when interpreting the results
20 of this study. Firstly, it is well known the DWI has noise and the dominant eigenvector may not
necessarily lie perfectly in the fibre orientation, however, we minimised these effects by
22 averaging two DWI sequences and the surrounding voxels in 3D. Future improvements may

include removing noise from the diffusion tensor to extract a vector field constrained by the architectural properties of skeletal muscles [24]. Secondly, the optimisation process was very sensitive to the initial guess, which had to be obtained from previous experiences with skeletal and cardiac muscle [25, 26]. The bounds place on the parameters ensured that the model converged numerically. Further, the constitutive law used in this study, the pole-zero, is a microstructural based law that is popular in cardiac and skeletal muscles as part of the Physiome Project [27]. However, it is known that other popular strain energy density functions are used, such as Mooney Rivlin, hence we have provided the raw strain energy density data as supplementary material for researchers to refit their own constitutive law parameters. Thirdly, our transducer was not MR compatible in this study, but there are MR specific transducers available in the market. If they were used in this presented rabbit rig then both shape and force measurements could be performed simultaneously without removing the rig from the MRI bore. However, the current study was best performed outside the MR as we measured the history of muscle force over 36 hours in order, to determine a steady state phase and peak force used as a surrogate for maximum contraction.

A key finding from this study was that steady state rabbit muscle force post rigor is a good surrogate for the *in vivo* state, especially at low deformations. When the deformation is higher we found a consistent ratio that may be used to scale the force to the *in vivo* state. The complete passive force curve during rigor was consistent with that reported by Van Ee et al. [6], however, in that study they did not consider different muscle lengths or provide a ratio between the passive and *in vivo* force. Moreover, during the onset and passing of rigor, the results exhibited a low standard deviation across both rabbits except during the descent phase. This region is highly variable and likely to be rabbit specific. The peak values during passive

contraction were chosen as a surrogate for the maximum contraction in our computational model based on the idea that during rigor the actin-myosin filaments shorten in a similar manner to what happens during active muscle contraction. In live muscle, adenosine triphosphate (ATP) enters the fibres leading to muscle contraction. This is then pumped out leading to a relaxation of the cross-bridges. Following death there is no energy to pump out the ATP leading to an increased contracted state. Eventually the fibres breakdown which leads to relaxation [28]. We have used this idea to get a surrogate measure of the active contraction at peak rigor as some of the cross-bridge kinetics is the same up to peak rigor.

The presented ‘pole zero’ parameters are useful for researchers evaluating passive muscle behaviour in rabbits and also for tendinopathy applications, typically assessed in rabbits [29, 30]. It was shown that the pole ($a_{\alpha\beta}$), which is the limit on the Green’s strain, was the most influential parameter through a sensitivity analysis, especially in the sheet and sheet-normal directions. Specifically, our value for a_{11} (fibre direction) was set to 1.0 based on previous skeletal modelling reported by Fernandez et al.[23, 25], where the human rectus femoris muscle was studied. Following optimisation we found that the pole in the transverse directions were $a_{22} = a_{33} = 0.097\sim 0.1$, which was slightly lower and stiffer than those reported in Fernandez et al. [23, 25], which used a value of $a_{22} = a_{33} = 0.4$. This is likely due to the human rectus femoris muscle being more compliant and less stiff than the rabbit gastrocnemius. The curvature ($b_{\alpha\beta}$) was set to 1.0 for numerical convergence stability for all three directions.

Inclusion of DWI fibres produced significantly different surface shape compared to parallel fibres, specifically on the medial head with differences up to 3.7 mm on the medial side. This side also accounted for larger non-uniform variations in strain. While the strain increased along the length of the muscle in both cases, the DWI informed muscle showed increased

variation medial to lateral (the muscle width). This pattern of non-uniform variation attributed to fibre orientation has also been reported by Blemker et al. [31]. The largest principal components of the strain aligned with the fibre direction, which highlights that the muscle is bulging in the muscle belly differently along the length, compared to the parallel fibre-based muscle. A celery gold standard with known parallel fibre orientation quantified a maximum error of 4.6° closest to the air water boundary. In practice, most of the useful information is well within the water volume and we would expect the error to be much lower. Further, a background threshold greater than 90 combined with a white matter FA greater than 0.1 gave the lowest error across the celery geometry. In practice, we found that a background threshold greater than 30 was more suitable as 90 typically produced a sparse data set and removed important fibre diffusion information in the rabbit muscle belly.

Acknowledgments

The authors would like acknowledge the financial assistance of an Aotearoa Bioengineering fellowship from the Robertson Foundation awarded to J Fernandez and an MBIE grant awarded to K Mithraratne (UOAX0712 and UOAX1006). We also kindly acknowledge Dr Beau Pontré and Ms Rachel Heron from the Centre for Advanced MRI for their help with imaging.

References

- 2 1. Alföldi, J., F. Di Palma, and K. Lindblad-Toh, *The European Rabbit Genome*, in *Rabbit Biotechnology* 2009, Springer. p. 129-129.
- 4 2. Herzog, W. and D. Longino, *The role of muscles in joint degeneration and osteoarthritis*. *Journal of biomechanics*, 2007. **40**: p. S54-S63.
- 6 3. Grover, D.M., A.A. Chen, and S.J. Hazelwood, *Biomechanics of the rabbit knee and ankle: Muscle, ligament, and joint contact force predictions*. *Journal of biomechanics*,
8 2007. **40**(12): p. 2816-2821.
4. Winters, T.M., et al., *Whole muscle length-tension relationships are accurately modeled
10 as scaled sarcomeres in rabbit hindlimb muscles*. *Journal of biomechanics*, 2011. **44**(1):
p. 109-115.
- 12 5. Davis, J., K.R. Kaufman, and R.L. Lieber, *Correlation between active and passive
isometric force and intramuscular pressure in the isolated rabbit tibialis anterior muscle*.
14 *Journal of biomechanics*, 2003. **36**(4): p. 505-512.
6. Komi, P., et al., *Optic fibre as a transducer of tendomuscular forces*. *European journal of
16 applied physiology and occupational physiology*, 1996. **72**(3): p. 278-280.
7. Sun, J.-S., et al., *Failure sites and peak tensile forces of the composite triceps surae
18 muscle by passive extension in the rabbit*. *Clinical Biomechanics*, 1994. **9**(5): p. 310-314.
8. Van Ee, C., A. Chasse, and B. Myers, *Quantifying skeletal muscle properties in
20 cadaveric test specimens: effects of mechanical loading, postmortem time, and freezer
storage*. *Journal of biomechanical engineering*, 2000. **122**: p. 9.
- 22 9. Bammer, R., et al., *Diffusion tensor imaging using single-shot SENSE-EPI*. *Magnetic
Resonance in Medicine*, 2002. **48**(1): p. 128-136.

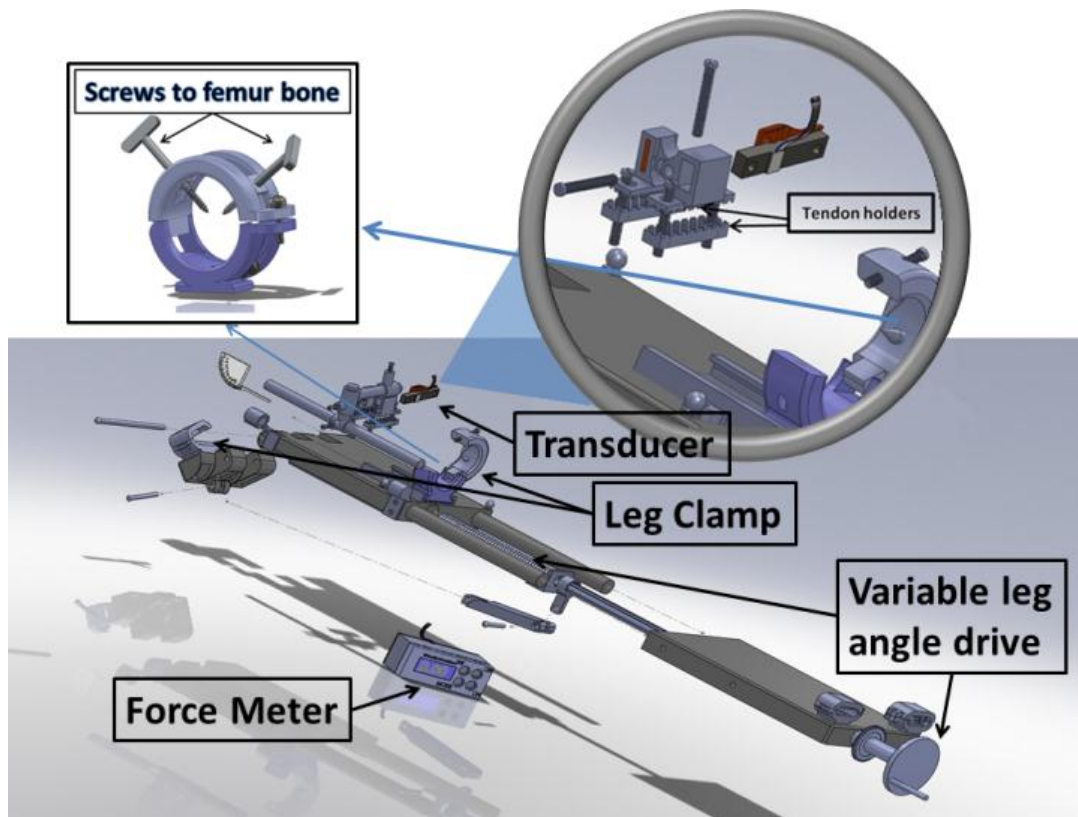
10. Hsu, E.W., et al., *Two-component diffusion tensor MRI of isolated perfused hearts*.
2 Magnetic Resonance in Medicine, 2001. **45**(6): p. 1039-1045.
11. Scollan, D.F., et al., *Histological validation of myocardial microstructure obtained from*
4 *diffusion tensor magnetic resonance imaging*. American Journal of Physiology-Heart and
Circulatory Physiology, 1998. **275**(6): p. H2308-H2318.
- 6 12. Basser, P.J. and C. Pierpaoli, *Microstructural and physiological features of tissues*
elucidated by quantitative-diffusion-tensor MRI. Journal of Magnetic Resonance-Series
8 B, 1996. **111**(3): p. 209-219.
13. Jones, D.K., et al., *Non-invasive assessment of axonal fiber connectivity in the human*
10 *brain via diffusion tensor MRI*. Magnetic Resonance in Medicine, 1999. **42**(1): p. 37-41.
14. Galban, C.J., et al., *Diffusive sensitivity to muscle architecture: a magnetic resonance*
12 *diffusion tensor imaging study of the human calf*. European journal of applied physiology,
2004. **93**(3): p. 253-262.
- 14 15. Damon, B.M., et al., *Validation of diffusion tensor MRI-based muscle fiber tracking*.
Magnetic Resonance in Medicine, 2002. **48**(1): p. 97-104.
- 16 16. Olsen, N.J., J. Qi, and J.H. Park, *Imaging and skeletal muscle disease*. Current
rheumatology reports, 2005. **7**(2): p. 106-114.
- 18 17. Van Donkelaar, C., et al., *Diffusion tensor imaging in biomechanical studies of skeletal*
muscle function. Journal of ANATOMY, 1999. **194**(1): p. 79-88.
- 20 18. Bradley, C., A. Pullan, and P. Hunter, *Geometric modeling of the human torso using*
cubic Hermite elements. Annals of Biomedical Engineering, 1997. **25**(1): p. 96-111.
- 22 19. Stejskal, E.O. and J. Tanner, *Spin diffusion measurements: Spin echoes in the presence of*
a time-dependent field gradient. The journal of chemical physics, 1965. **42**: p. 288.

20. Bassar, P.J. and C. Pierpaoli, *Microstructural and physiological features of tissues elucidated by quantitative-diffusion-tensor MRI*. Journal of Magnetic Resonance, Series B, 1996. **111**(3): p. 209-219.
21. Hunter, P., S. Sideman, and H. Fozzard, *Myocardial constitutive laws for continuum mechanics models of the heart*. Advances in experimental medicine and biology, 1995. **382**: p. 303-318.
22. Babarenda Gamage, T.P., et al., *Identification of mechanical properties of heterogeneous soft bodies using gravity loading*. International journal for numerical methods in biomedical engineering, 2011. **27**(3): p. 391-407.
23. Fernandez, J. and P. Hunter, *An anatomically based patient-specific finite element model of patella articulation: towards a diagnostic tool*. Biomechanics and modeling in mechanobiology, 2005. **4**(1): p. 20-38.
24. Levin, D.I.W., et al., *Extracting skeletal muscle fiber fields from noisy diffusion tensor data*. Medical Image Analysis, 2011.
25. Fernandez, J. and M. Pandy, *Integrating modelling and experiments to assess dynamic musculoskeletal function in humans*. Experimental physiology, 2006. **91**(2): p. 371-382.
26. Hunter, P., A. McCulloch, and H. Ter Keurs, *Modelling the mechanical properties of cardiac muscle*. Progress in biophysics and molecular biology, 1998. **69**(2): p. 289-331.
27. Hunter, P.J. and T.K. Borg, *Integration from proteins to organs: the Physiome Project*. Nature Reviews Molecular Cell Biology, 2003. **4**(3): p. 237-243.
28. Smith, E.C.B., *Changes in elasticity of mammalian muscle undergoing rigor mortis*. The Journal of Physiology, 1939. **96**(2): p. 176.

29. Sharma, P. and N. Maffulli, *Tendon injury and tendinopathy: healing and repair*. The
2 Journal of Bone & Joint Surgery, 2005. **87**(1): p. 187-202.
30. Wang, C.J., et al., *Shock wave therapy induces neovascularization at the tendon–bone
4 junction. A study in rabbits*. Journal of orthopaedic research, 2003. **21**(6): p. 984-989.
31. Blemker, S.S., P.M. Pinsky, and S.L. Delp, *A 3D model of muscle reveals the causes of
6 nonuniform strains in the biceps brachii*. Journal of biomechanics, 2005. **38**(4): p. 657-
665.
- 8 32. Hunter, P.J., *Myocardial constitutive laws for continuum models of the heart*, in
Molecular and subcellular cardiology, B.R. Sidman S, Editor 1995: New York:. p. 303-
10 318.
33. Hunter, P.J., *Myocardial constitutive laws for continuum mechanics models of the heart*,
12 in *Molecular and subcellular cardiology*1995, Springer. p. 303-318.
- 14
- 16
- 18
- 20
- 22

Tables and Figures

2



4

Figure 1: MRI compatible rabbit rig used to dorsiflex the rabbit hind limb within the MRI bore and measure gastrocnemius tendon force for each foot position.

6

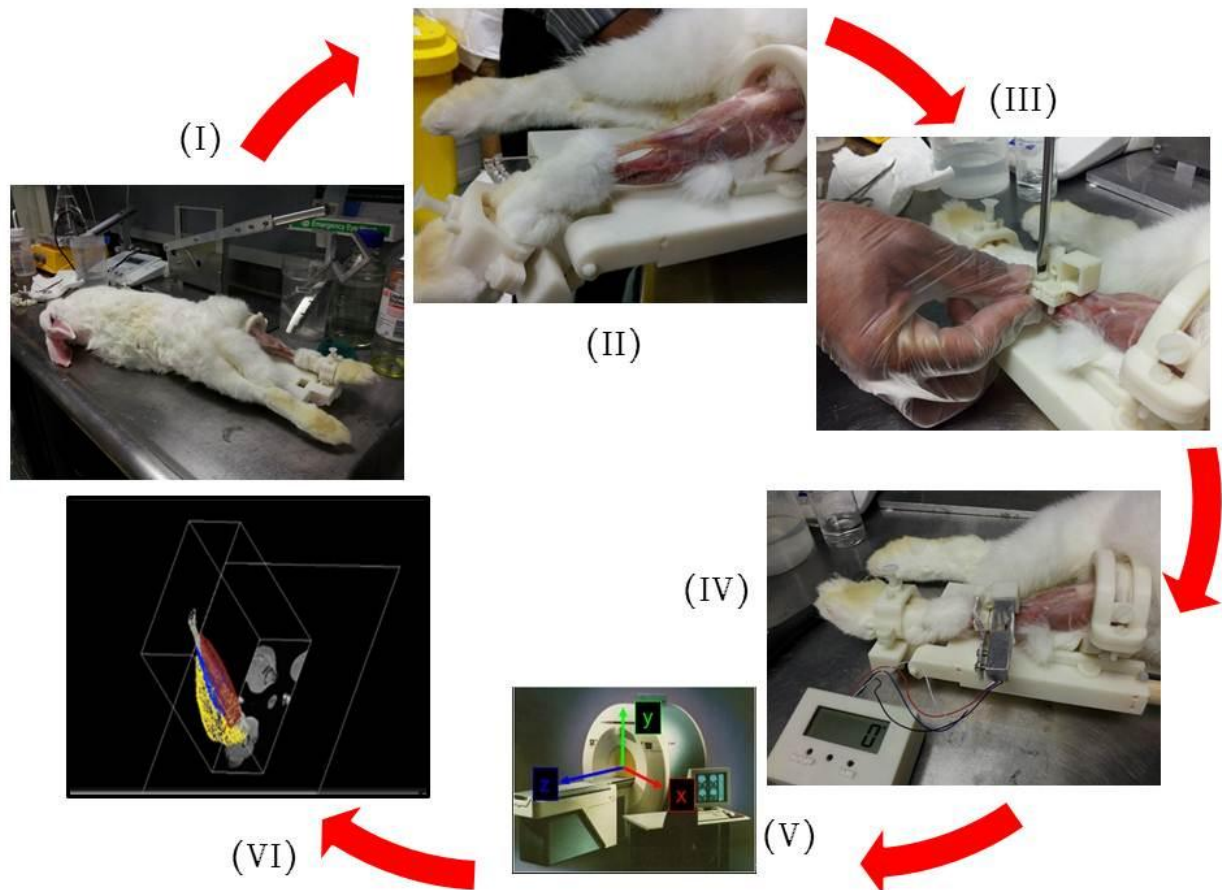
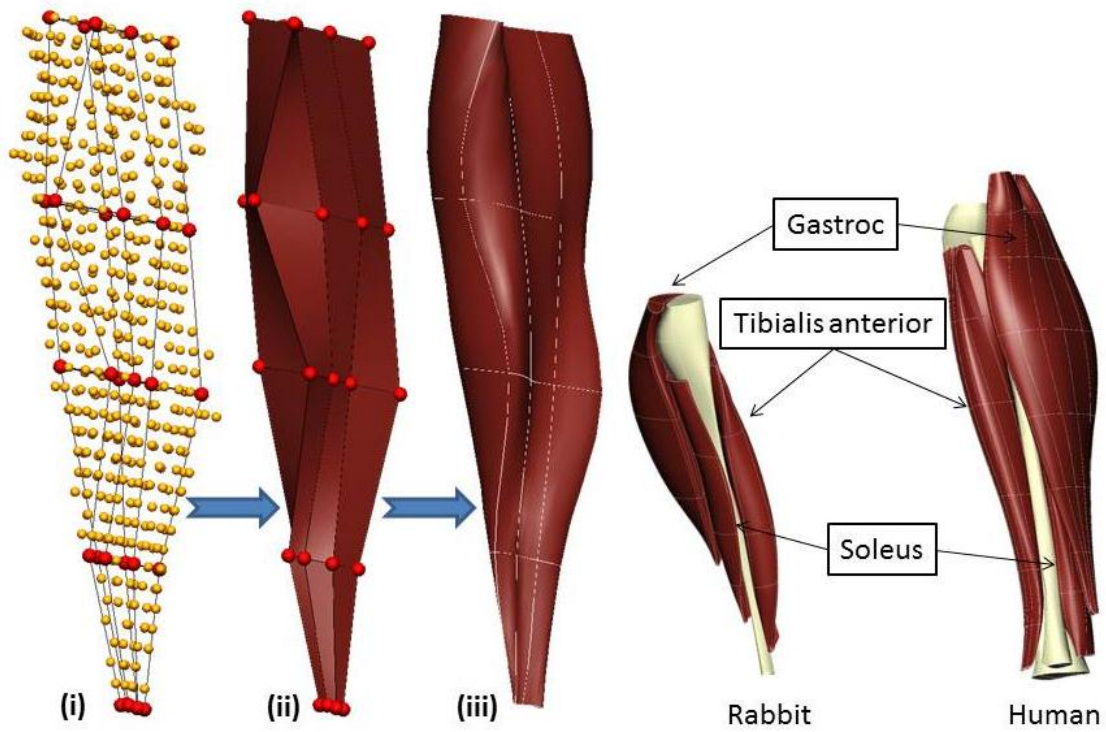
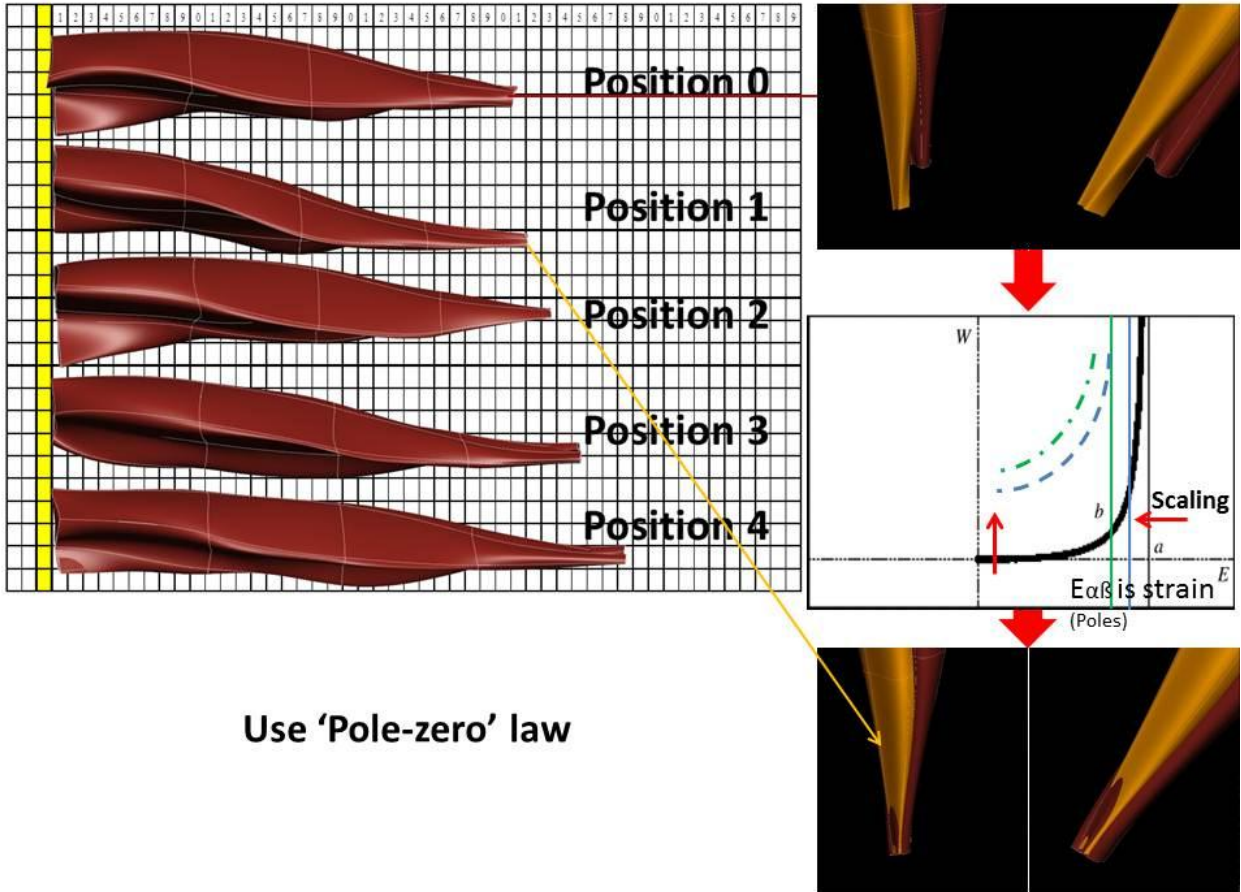


Figure 2. (I & II) The experiment framework. (III & IV) The rabbit fixated on the rig; connecting the transducer; (V) MR imaging and (VI) digitised T1 images for geometry creation.

2
4
6

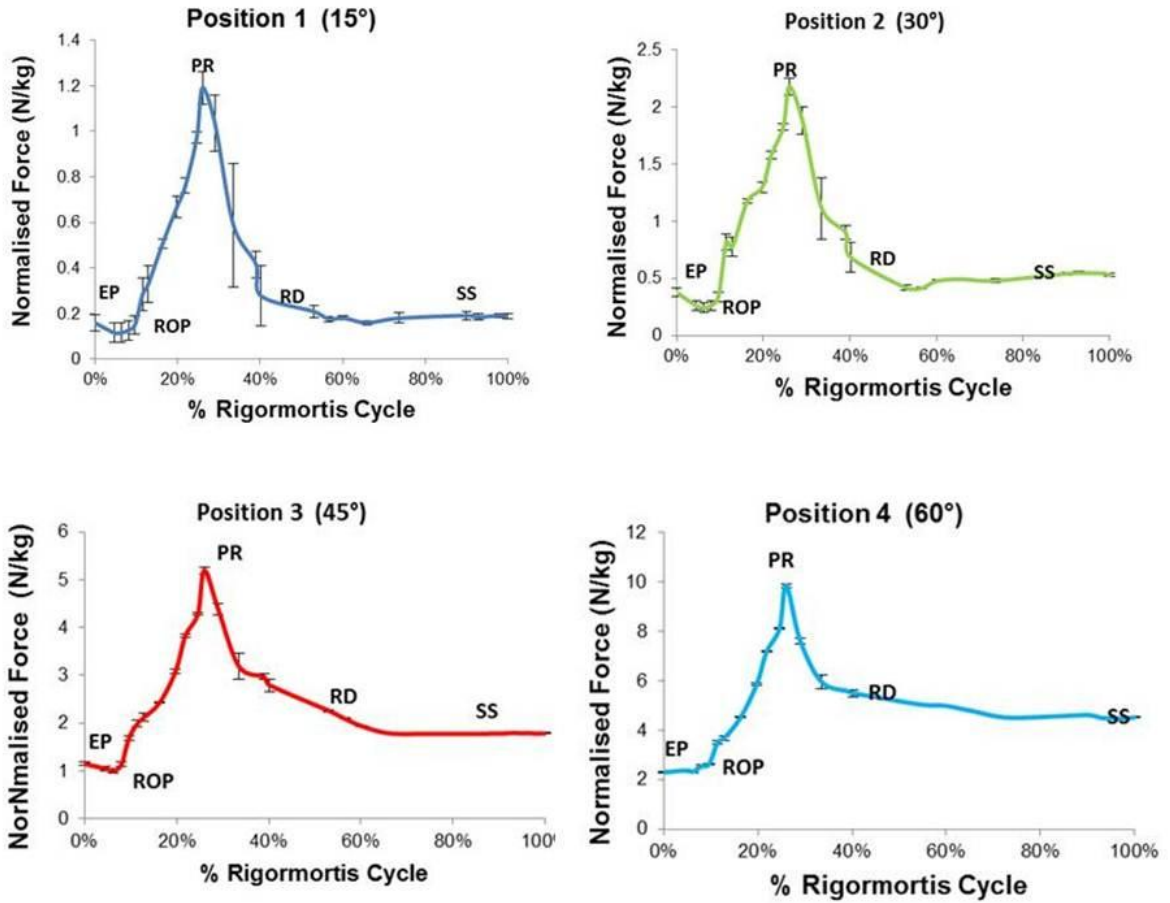


2 Figure 3. High-order finite element model of rabbit hind limb developed from rabbit MRI; and similar
4 human model developed using the same techniques.
6



2 Figure 4: Relaxed and four MR derived muscle deformations; and muscle optimised (red) to match experimental gold standard (gold) using 'pole zero' constitutive law.

4



2 Figure 5. The average force in all positions for 2 rabbits (mean \pm 1 standard deviation). The stages were
 4 EP (euthanised point), ROP (rapid rigor onset point), PR (peak rigor point), RD (steady rigor decrease
 point), SS (steady state point).

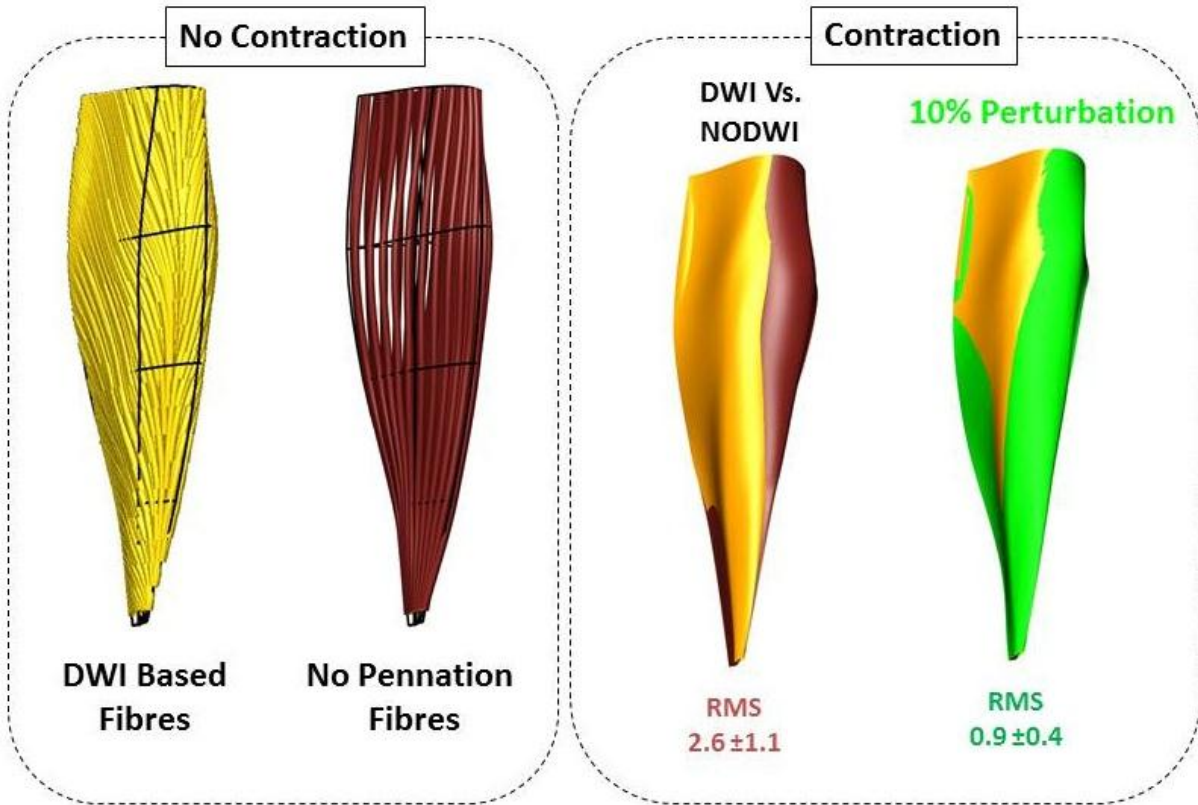
6

8

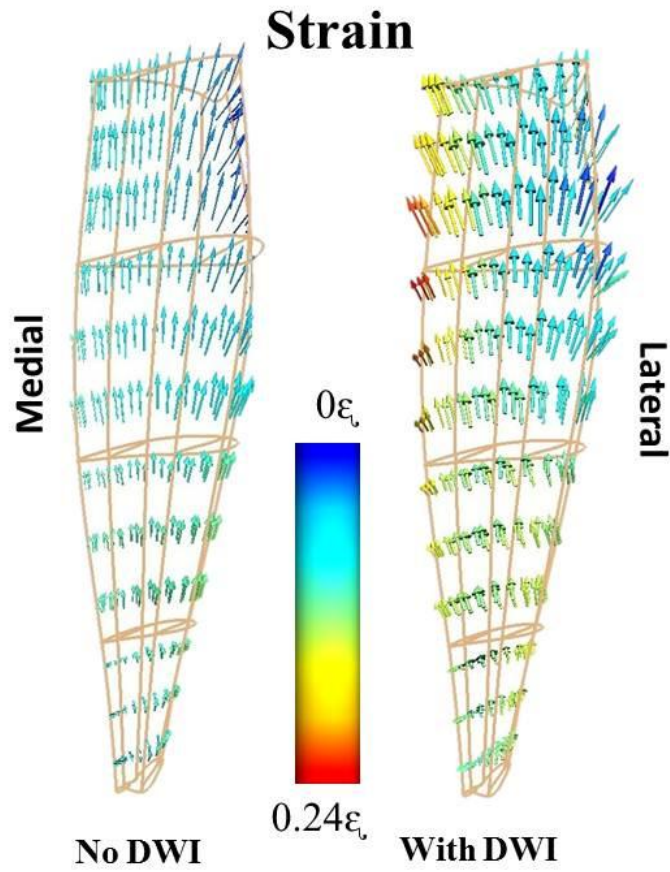
10

12

14



2 Figure 6: (Left) Fitted DWI fibres (gold) contrasted with no pennation based fibres. (Right) DWI
4 contractile shape overlaid with no pennation contractile shape and effect of 10% perturbation in fibre
angle (green/gold).



2 Figure 7: Muscle strain with and without DWI when in maximum muscle contraction.

4



6 Figure 8: Phantom Celery to validate the process of the study.

8

Tables:

Table 1: Siemen’s 4.7 T MRI T1 settings for muscle boundary geometries.

Echo Time (TE)	10 ms
Repeat Time (TR)	1000 ms
Number of Excitations (NEX)	2
Resolution	2 x 0.9 x 0.9 mm

Table 2: Siemen’s 4.7 T MRI DWI settings for fibre information

Echo Time (TE)	40 ms
Repeat Time (TR)	3000 ms
Number of Excitations (NEX)	2
Number of gradient Directions	20 + 1
b-Value	500 s/mm ²
Resolution	2 x 0.9 x 0.9 mm

Table 3: Optimised ‘pole-zero‘ material parameters satisfying all deformed positions including DWI pennation fibres

	Coefficient	Pole	Curvature
Fibre	0.01	1	1
Sheet	0.221	0.097	1
Sheet-normal	0.221	0.097	1

Table 4: Root Mean Square error of predicted muscle shape versus experimental gold standard across all four deformed positions for the first and second rabbit.

Position	First Rabbit	Second Rabbit
P1	1.57949 E+00	1.47588 E+00
P2	1.70629 E+00	2.37578 E+00
P3	1.14973 E+00	1.70237 E+00
P4	1.54098 E+00	1.04943 E+00
Average	1.49412 E+00	1.65087 E+00

Table 5: Sensitivity test for pole-zero parameters

Sensitivity Test	
Optimal	% Error
$k_{11} + 10\%$	0.00%
$a_{11} + 10\%$	0.27%
$b_{11} + 10\%$	0.0%
$k_{22} + 10\%$	0.65%
$a_{22} + 10\%$	11.18%
$b_{22} + 10\%$	1.67%
$k_{33} + 10\%$	0.38%
$a_{33} + 10\%$	14.15%
$b_{33} + 10\%$	0.97%

2

4

6

8

10

12

14

16

18

20

22

24

26

28

30

32

34

Appendix A

The weak form of the governing equation used for solving the finite elastic mechanics is given by

$$\int_{V_o} \frac{1}{J} T^{\alpha\beta} F_{\beta}^j \frac{\partial \delta u_j}{\partial v_{\alpha}} dV_o = \int_{S_c} f_c \delta u_j^c dS_c, \quad (A1)$$

since the gastrocnemius muscle is undergoing large strain (greater than 10%). V_o is the undeformed volume and S_c is the surface in contact used to account for the interaction between muscles and the tibia. δu_j is the virtual displacement, δu_j^c is the variation of the contact gap and

$F_{\beta}^j = \partial x_j / \partial v_{\beta}$ is the deformation gradient tensor which maps between the deformed spatial coordinates x_j , and material coordinates, v_{β} . The Jacobian, J , is the determinant of the deformation gradient tensor, F and f_c is the frictionless contact force, which is implemented using a penalty based method with the complete details described in Fernandez et al.[23]. $T^{\alpha\beta}$ is the 2nd Piola-Kirchoff stress tensor,

$$T^{\alpha\beta} = \frac{\partial W}{\partial E_{\alpha\beta}} + p a_v^{\alpha\beta} + T_0 \delta_1^{\alpha} \delta_1^{\beta}, \quad (A2)$$

and is defined with respect to the undeformed curvilinear material coordinate system, v_{α} . W is a strain energy density function and $E_{\alpha\beta}$ are the Green-Lagrange strain components. The hydrostatic pressure, p , arises in order to satisfy volume conservation and T_0 is the second Piola Kirchoff equivalent of the Cauchy active stress (muscle contraction). The contravariant metric tensor $a_v^{\alpha\beta} = \partial v_{\alpha} / \partial x_k \cdot \partial v_{\beta} / \partial x_k$ is the inverse of the right Cauchy deformation tensor (covariant

metric tensor). For muscle contraction we used the model of Hunter [26] and added a contractile

2 force in the DWI informed fibre direction to simulate muscle action given by:

$$\sigma_0(\lambda, Ca_{actm}) = \frac{(Ca_{actm} \cdot [Ca^{2+}]_{\max})^h}{(Ca_{actm} \cdot [Ca^{2+}]_{\max})^h + (c_{50})^h} \cdot \sigma_{ref} [1 + \beta(\lambda - 1)], \quad (A3)$$

4 Where σ_0 is the active tension added to the fibre direction and given by the calcium-tension

derived from the ‘fading-memory’ model, which is based on the Hill type model [32, 33]. Ca_{actm}

6 is the level of activation (non-dimensional calcium value), λ is the sarcomere stretch length,

$[Ca^{2+}]_{\max}$ is the intracellular calcium concentration for maximum activation, c_{50} is the

8 concentration at which isometric tension is 50% of its maximum, h is the Hill coefficient, T_{ref} is

the active isometric tension when $\lambda = 1$ and β is the slope parameter.

10